Journal of Materials Chemistry B

ROYAL SOCIETY OF CHEMISTRY

PAPER

View Article Online
View Journal | View Issue

Cite this: J. Mater. Chem. B, 2025, 13, 13088

A new multifunctional copper iodide–pyrazine hybrid for sensitive creatinine detection in biological samples: synthesis, structural features, characterization, and electrochemical evaluation

Wissem Hallab,[a] Ahlem Guesmi,[b] Raja Jlassi,[a] Jassem Wannassi,[c] Noureddine Mhadhbi,[a] Abdellah Tahiri,[d] Wesam Abd El-Fattah,[b] Naoufel Ben Hamadi,[b] Houcine Barhoumi[c] and Houcine Naïli *[a]

Received 30th April 2025,
Accepted 8th September 2025

DOI: 10.1039/d5tb01035g

rsc.li/materials-b

The organic–inorganic hybrid compound [Cu_2I_2(μ-pyrazine)] was synthesized *via* a hydrothermal method and characterized using X-ray diffraction (XRD), infrared (IR) and Raman, UV–visible, and X-ray photoelectron (XPS) techniques. The compound crystallizes in a triclinic system and forms a 2D staircase-like framework. Optical measurements indicate a direct bandgap of 0.95 eV, suggesting semiconducting behavior and potential applicability as a biological sensor. Furthermore, electrodes modified with [Cu_2I_2(μ-pyrazine)] were evaluated for creatinine detection, exhibiting high sensitivity and selectivity, with a detection limit as low as 1×10^{-8} M. The sensor also demonstrated excellent stability and reproducibility in real sample analyses, achieving recovery rates between 90.3% and 103.9%. These findings highlight the multifunctionality and potential of this hybrid material for applications in both clinical diagnostics and environmental monitoring.

Introduction

Coordination complexes have fascinated chemists and material scientists for decades because their properties, such as topology, morphology, optical behavior, and photophysical traits, can be finely adjusted.[1–5] Pyrazine–copper halide complexes, in particular, are an intriguing group of materials that combine the unique characteristics of nitrogen-rich heterocyclic ligands with halide-containing metals.[6–8] This combination leads to unique coordination frameworks with diverse applications, including gas storage and separation, magnetism, optical technologies, *etc.*[9–12] The core appeal of metal–organic frameworks (MOFs) lies in their remarkable crystal engineering, which enables the formation of diverse extended framework structures.[13] These outstanding architectures are constructed by linking tetrahedral or octahedral metal cation centers with ligands and anion systems whose roles such as coordination arrangement, functional properties, steric and electronic effects, size, and ligand-binding ability collectively determine the topology (dimensionality) of the structures formed.[7,14–16]

Depending on the reaction conditions, pyrazine–Cu complexes can be synthesized through various methods, such as hydrothermal or solvothermal synthesis, microwave-assisted synthesis, and solvent-free transformations, each offering unique advantages in terms of structural control, yield, and material properties.[17,18] Significant attention has been given to this subject because it marks a progression toward "green chemistry", addressing environmental and public health concerns through less hazardous and lower-cost chemical procedures.[19]

Extensive research has been conducted on copper (both Cu(I) and Cu(II)) coordination hybrid materials.[3,6,8,12] These materials utilize a variety of bridging organic ligands, particularly monodentate or bidentate N-donor ligands (such as pyridine, pyrazine and their derivatives, thiourea derivatives, carboxamide, *etc.*),[6,9,20,21] along with inorganic structural motifs involving rhombus-shaped dimer units, zig-zag chains, staircase chains, *etc.*, to give rise to coordination polymers exhibiting 1D, 2D, and 3D structural frameworks.[7,10,22]

As an example, within copper(I) pyrazine carboxamide complexes,[6] pyrazine generally functions as a monodentate ligand. However, exceptions exist, such as the Cu(pyrazine carboxamide)Br complex, which features both N- and N,O-coordinated pyrazine ligands. Compounds containing halides, nitrates, or perchlorates often act as bridging ligands, leading to the formation of polymeric structures. For instance, Cu(pyrazine carboxamide)$_2$I forms a zigzag

[a] Laboratory Physical-Chemistry of the Solid State, Department of Chemistry, Faculty of Sciences of Sfax, University of Sfax, BP 1171, Sfax 3000, Tunisia. E-mail: houcine_naili@yahoo.com, houcine.naili@fss.rnu.tn
[b] Chemistry Department, College of Science, Imam Mohammad Ibn Saud Islamic University (IMSIU), P.O. Box 5701, Riyadh 11432, Saudi Arabia
[c] Laboratory of Interfaces and Advanced Materials, Faculty of Sciences, University of Monastir, 5019 Monastir, Tunisia
[d] Laboratory ISTM, Department of Physics, Faculty of Sciences, Chouab Doukkali University, El Jadida 24000, Morocco

polymeric chain, with copper and iodine atoms alternating in an approximately tetrahedral coordination geometry, connected by hydrogen bonds (N–H···O) between pyrazine molecules, resulting in a two-dimensional network.[6]

Considering the study on copper(I) halide coordination polymers with monodentate ligand $[CuIL]_n$ (L = 3- and 4-benzoylpyridine) and bidentate ligand $[Cu_2I_2L]_n$ (L = pyrazine, quinazoline) ligands.[10] The $[Cu_2I_2(quinz)]_n$ complex exhibits a double-stranded stair-like structure, where copper is 4-coordinate, bonded to three iodine atoms and the nitrogen of a single ligand, resulting in a distorted tetrahedral geometry. Copper bromide analogues form either a 'zigzag' chain or 'ladder' structure may form, with the ligand coordinating to the metal either in a bidentate mode bridging two rungs of the ladder binding in a monodentate manner, as seen in $[CuI(3\text{-bzpy})]_n$. These complexes also exhibit short Cu–Cu bond lengths, measuring 2.65 Å for $[Cu_2I_2(quinz)]_n$ and 2.68 Å for $[CuI(3\text{-bzpy})]_n$, accompanied by weakened π–π stacking interactions.[10]

Recent advances in electrochemical sensors for analytical applications have been greatly influenced by the introduction of nanomaterials and hybrid materials.[23] Today, a wide range of high-performance nanomaterials can be synthesized using various innovative techniques. Progress in synthesis methods, coupled with a deeper understanding of the structure and properties of nanomaterials,[24] has significantly enhanced the quality of analytical applications.[25] Recent efforts in developing multifunctional nanomaterials have increasingly focused on inorganic–organic hybrid materials,[26] which offer efficient catalytic properties, large surface areas, and superior adsorption capabilities. Additionally, large-capacity functional materials contribute to improved stacking efficiency,[26] while precious metals are widely utilized for their exceptional catalytic properties,[27] further advancing the performance of electrochemical sensors.

Electrochemical sensors have garnered significant attention in recent years due to their numerous advantages, including high sensitivity, rapid response, low detection limits, portability, and cost-effectiveness.[23,24] These devices operate based on direct electrical signal transduction, which allows real-time monitoring and facile miniaturization.[25] Furthermore, the integration of nanostructured and hybrid materials into electrode design enhances their surface area, conductivity, and selectivity, making them highly effective for detecting trace-level analytes in complex matrices.[26] Owing to their adaptability and compatibility with diverse targets, electrochemical sensors have emerged as powerful tools in biomedical diagnostics, environmental monitoring, and food safety analysis.[27]

This article investigates the synthesis, structural characteristics, and multifunctional properties of pyrazine–copper iodide complex. By linking fundamental research with application-driven studies, it underscores the promising potential of these materials in biomaterials science. To evaluate their practical utility, a novel hybrid material was developed and assessed as a sensitive electrochemical sensor. In particular, a $[Cu_2I_2(\mu\text{-pyrazine})]$-modified glassy carbon electrode (GCE) was fabricated and effectively employed for the detection of creatinine.

Experimental section

Materials

The reagents used in this study include creatinine, ethanol (≥96%), sodium hydroxide, uric acid (UA), cysteine (Cys), ascorbic acid (AA), dopamine (DA), and glucose, all sourced from Sigma-Aldrich, as well as products from Chimisi and Chimie Tunisie companies in Tunisia. Prepared by dissolving 0.1 M monosodium dihydrogen phosphate trihydrate ($KH_2PO_4 \cdot 3H_2O$, ≥99%) and 0.1 M disodium hydrogen phosphate dodecahydrate ($Na_2HPO_4 \cdot 12H_2O$, 99.998%) in distilled water, a 0.1 M phosphate buffer solution (PBS) at pH 7.4 was obtained.

The electrochemical measurements were performed using an Autolab PG potentiostat/galvanostat (AUT 83965), with control *via* the Autolab NOVA 2.1.6 software (Metrohm, Switzerland). These experiments were conducted in a conventional three-electrode electrochemical cell, where the working electrode was a $[Cu_2I_2(\mu\text{-pyrazine})]$-modified glassy carbon electrode (GCE), the reference electrode was an Ag/AgCl/KCl electrode, and the auxiliary electrode was a platinum wire with a diameter of 1 mm.

Synthesis of pyrazine–copper complex

The synthesis of the pyrazine–copper iodide complex was meticulously performed to ensure high purity and reproducibility. Hydrothermal synthesis was employed, involving the controlled reaction of copper(II) iodide, pyrazine ligands, and an iodine source (HI acid) within a high-pressure, high-temperature environment at 140 °C for 72 hours. Copper(II) iodide (0.25 g) was carefully dissolved in a mixture of deionized water and DMF solvent to create a homogeneous solution. To this solution, pyrazine (0.08 g) dissolved in a separate mixture of deionized water and DMF solvent was added under continuous stirring to facilitate effective coordination without additional heating. A few drops of HI acid were then introduced, and the resulting solution was transferred into a sealed autoclave. This technique facilitated the crystallization of the copper–pyrazine–iodide framework by promoting the dissolution and reaction of the precursors in an aqueous medium under controlled hydrothermal conditions. After the reaction, the solution was allowed to cool to room temperature and left undisturbed to promote crystal growth.

X-ray diffraction analysis

A thorough characterization of the synthesized complex was performed using advanced analytical techniques, beginning with single-crystal and powder X-ray diffraction (XRD) analysis. Data were collected using a SuperNova single-source at offset Eos diffractometer equipped with a Mo-Kα radiation source. The triclinic crystal structure was solved and refined using the SHELXT 2018/2 and SHELXL 2018/3 packages (Sheldrick, 2018/2015) within the Olex2 1.5 software (Dolomanov *et al.*, 2009).

Full-matrix least-squares minimization on F^2 was employed to achieve precise structural refinement. Hydrogen atoms were placed geometrically and constrained to ride on their respective parent atoms, with C–H = 0.95 Å and U_{iso} = 1.2U_{eq} (parent atom). The highest electron density peak was found 0.81 Å from atom I1, while the deepest electron density hole was located 0.79 Å from atom I1. Comprehensive details regarding the crystallographic data collection and refinement parameters are provided in Table S1. CCDC contains the supplementary crystallographic data for the title compound.

Spectroscopic studies

IR was employed to identify characteristic vibrational modes associated with the functional groups in the complexes (SI). The IR spectra were recorded using a PerkinElmer Spectrum 100 FTIR spectrometer, operating within the range of 400–4000 cm^{-1}. Raman effects are observed when monochromatic light interacts with a sample using the spectroscopic analysis device Lab Ram HR 800 in the range 50–3500 cm^{-1} (SI). The optical parameters, which highlight the optical properties intrinsic to the molecular structure, were determined using a Varian Cary 5000 double-beam spectrophotometer equipped with an integrating sphere, operating in the 200–1200 nm range (SI). Thermo-Fisher apparatus with Al K source with energy of 1486.6 eV was used to perform X-ray photoelectron spectroscopy (XPS) to investigate the chemical states of the elements in the sample. Electron and argon flood guns were used to compensate for the static charge buildup of the powders. The composition was determined using the manufacturer sensitivity factors (SI).

Electrochemical sensor and fabrication

Prior to surface modification, the glassy carbon electrode (GCE) was meticulously polished with 0.05 μm alumina powder. This polishing process aimed to achieve a mirror-like surface, effectively eliminating surface impurities and ensuring a smooth, clean electrode interface. After polishing, the electrode was thoroughly rinsed with ethanol followed by distilled water for 5 minutes to remove any residual alumina particles and contaminants. Subsequently, cyclic voltammetry (CV) was performed in a 5 mM $[Fe(CN)_6]^{3-/4-}$ solution containing 0.1 M KCl at a scan rate of 100 mV s^{-1}. The recorded voltammogram exhibited a stable and reversible redox response, confirming the electrode's suitability for subsequent surface modification. For the preparation of the modifier, 1 mg of $[Cu_2I_2(\mu\text{-pyrazine})]$ was dispersed in 1 mL of ethanol and subjected to ultrasonication for 20 minutes to ensure a homogeneous suspension. A measured aliquot of this well-dispersed suspension was drop-cast onto the pretreated GCE surface. The modified electrode was then allowed to dry at room temperature for 3 hours to ensure complete solvent evaporation and adherence of the material to the electrode surface.

Serum sample collection and ethical statement

Human serum samples were collected from voluntary adult donors under the supervision of a medical biologist. The collection and use of the samples were conducted in accordance with the ethical principles of the Declaration of Helsinki. Participation was voluntary, and donor anonymity and confidentiality were ensured throughout the research. The study received the required institutional approvals, and in accordance with the submitted ethics confirmation, we affirm that both ethical approval and informed consent were obtained prior to all experiments involving human participants. Two serum samples were used in this work: serum 1, collected from a healthy male volunteer aged 28 years, with no reported history of renal or metabolic disorders; and serum 2, collected from a healthy female volunteer aged 34 years, with no known clinical conditions or medication use. The samples were used exclusively for evaluating the electrochemical performance of the synthesized copper–pyrazine hybrid material in creatinine detection.

Results

Symphony of atoms

Using X-ray diffraction data, the crystal structure of the two-dimensional polynuclear $[Cu_2I_2(\mu\text{-pyrazine})]$ complex was determined. Initially, the structure was established using the heavy atom approach and subsequently refined using the least squares method. The refinement process resulted in final values of R_1 = 0.0179 and wR_2 = 0.0393 for a total of 1184 independent reflections with $I > 2\sigma(I)$, as outlined in Table S1 which summarizes the crystal data and X-ray experimental details of the compound, and the fractional atomic coordinates, isotropic or equivalent isotropic displacement parameters, and anisotropic displacement parameters related to this material are provided in Tables S2 and S3.

The complex crystals exhibit a triclinic crystal system and belong to the centrosymmetric space group $P\bar{1}$ (C_i^1), characterized by specific dimensions and angles: a = 4.1476(3) Å, b = 7.0776(7) Å, and c = 8.0489(6) Å; α = 109.478(8)°, β = 101.221(6)°, and γ = 97.174(7)°, with a molecular unit of Z = 1. All the atoms in this structure are located at the 2i Wyckoff site. The structural analysis of the crystal uncovered the presence of half of the Cu cations, one iodide anion, and half of the centrosymmetric (D_{2h}) bidentate pyrazine ligand within its formula unit (Fig. 1(a)). In accordance with the rule of charge balance, the Cu atom exhibits a valence of 1^+. In order to furnish a more comprehensive description of the structure, the Fig. 1(b) depicts the representative view of the copper coordination environment. This demonstration illustrates that the emergence of the $(CuI)_\infty$ cores pattern occurs as a direct, straightforward, result of the architect of the ligands. Moreover, the b-axis projection of the structure (Fig. 2), indicates the presence of planes comprising copper(I) atoms interconnected by nitrogen-donating heterocyclic ligands (pyrazine) and iodine bridges, where each of these metal centers displays crystallographically unique tetrahedral coordination geometry.

The coordination mode of the mineral ligands within the complex represents a significant structural feature of this

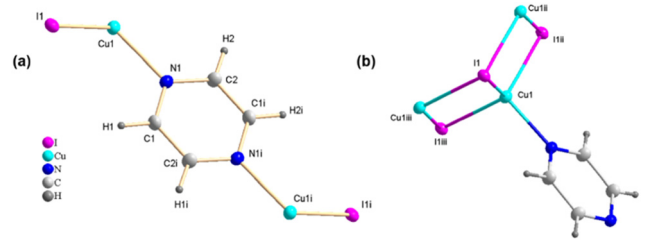

Fig. 1 (a) Formula unit of the $[Cu_2I_2(\mu\text{-pyrazine})]$ complex and (b) copper coordination environment. Symmetry codes: (i) $1-x, 1-y, 2-z$; (ii) $1-x, -y, 1-z$. (iii) $-x, -y, 1-z$.

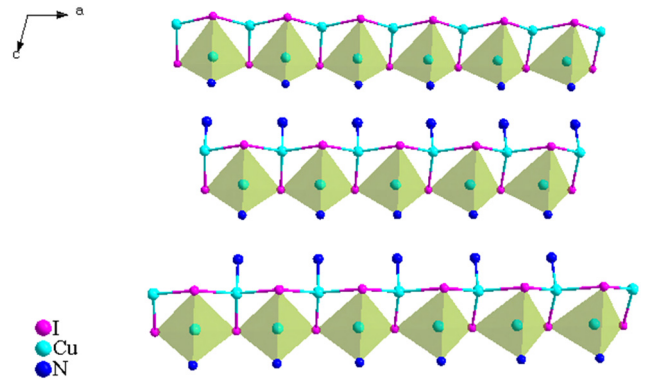

Fig. 2 Connectivity in a staircase-like pattern, composed of distorted CuI_3N tetrahedra.

system, every distinct copper ion is 3-fold stitches with a specific μ_3-I^- connectivity mode to the adjacent iodide ions with spanning distances of Cu–I = 2.6291(16) to 2.6494(16) Å, and all the three iodine ions are also bridged to three cuprous ions μ_3-Cu, leaving a single vacancy site in the coordination sphere, a nitrogen donor from the organic molecule (1,4-diazine) occupies this remaining fourth site, forming a stable and distorted tetrahedral geometry CuI_3N, this finding is consistent with the four-coordinate geometry distortion index (τ_4) that indicates a value of approximately 0.89 (for which a value of 1.00 is characteristic of an ideal tetrahedron), as derived from the equation (eqn (1)) provided by L. Yang and his co-workers:[28]

$$\tau_4 = \frac{360 - (\alpha + \beta)}{141^\circ} \quad (1)$$

The terms α and β refer to the two largest angles formed between ligands and the metal ion within the coordination sphere (ligand–metal–ligand angles). These angles are crucial in describing the geometry of the coordination complex and can provide insights into its overall structure and stability. Aside from the function of the halide ligands, the N atoms within this arrangement play a crucial role in structuring the crystal lattice and serve to link adjacent (CuI) step-polymers, with specific bond distances and angles provided: Cu–N = 2.049(2) Å and N–Cu–I angles range from 105.04(7) to 108.31(7)° (Table S4), thereby facilitating the formation of the planar two-dimensional sheets (Fig. 3).

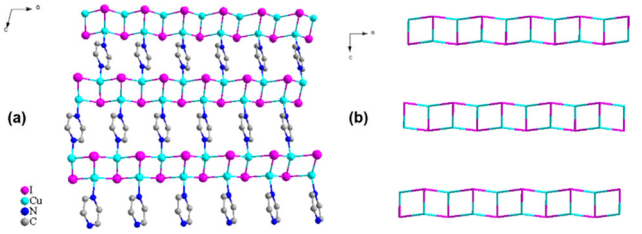

Fig. 3 (a) 2D framework and (b) 2D staircase-like motif (H atoms omitted for clarity).

Based on the Cu···Cu intra-$(CuI)_\infty$ separation distances, which range from 2.7454(7) to 2.7651(6) Å, and a mean angle of 58.495° observed between adjacent Cu_2I_2 units tilted toward each other (Table S4), it is evident that the structural arrangement adopts a two-dimensional staircase motif within the polymer (Fig. 3).[7,29] This entails that the contiguous layers are packed in a staggered manner, ensuring that the assembly of the alternating CuX (X = I) cluster columns is shifted by half a translation with respect to each other, and their orientation changes alternately along the chain (up and down) (Fig. 3). This efficient arrangement of crystals is primarily caused by the coordinating tails (N–Cu–I) of the stacked bridging ligands between the inorganic modules, oriented in opposite directions (Fig. 1(a)). In fact, the ligating molecules maintain their planarity and stack along both sides of the CuI skeleton, with an interplanar distance of 6.8999(9) Å (inter-$(CuI)_\infty$ separation distance) (Fig. 3). Consistent with literature findings, robust π–π interactions typically occur at a distance of approximately 3.8 Å, while weaker interactions tend to occur beyond 3.6 Å.[7] In this particular case, the distance between the rings is relatively long at 4.1476(3) Å, indicating a weak π–π interaction (Fig. 4). This elongated alignment suggests that mutual repulsion and steric hindrance between the rings are significant factors in shaping the structure.[7,30] Cuprophilic interactions are also evident within this cluster, as evidenced by the average Cu–Cu distances of 2.7552 Å, which fall below the combined van der Waals radii of copper atoms (2.80 Å) suggesting a subtle metal–metal interplay. These distances are comparable to, and slightly longer than, those observed previously (2.648 (2) Å).[31] This observation is particularly notable when compared to the longer distances found in extended [CuBr] units (3.985 Å).[29]

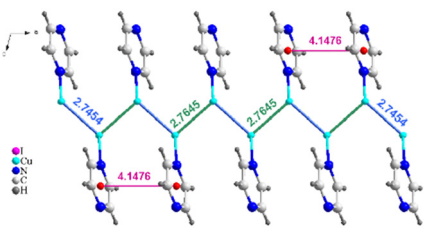

Fig. 4 π–π Interactions between pyrazine, layer spacing, and zigzag cuprophilic (Cu···Cu) interactions.

This suggests the presence of weak metal–metal bonding between the $[Cu_2I_2]$ units.

Summarizing our crystallographic inquiries, the compound exhibits a deformed geometry around the Cu atom, mostly due to the I–Cu–I angles spanning from 103.50(6) to 117.32(4), and the N–Cu–I angles as previously mentioned. These tetrahedra are connected into a 2D CuI staircase chain built of the alternating Cu–I corrugated sequences that are parallel to the ac crystallographic plane and stack along the crystallographic b direction (Fig. 3), linked by pyz ligands giving rise to an infinite chain of $[Cu_2I_2(\mu\text{-pyrazine})]_n$. The related system of the novel polymer exhibits isostructural characteristics with its closest chloride-based analogues,[32] revealing a ladder-like structure (Cu_2I_2) when pyz is employed in this reaction.

Electrochemical analysis of $[Cu_2I_2(\mu\text{-pyrazine})]$-modified GCE

The electrochemical behavior was thoroughly examined using cyclic voltammetry (CV) and electrochemical impedance spectroscopy (EIS) of both the bare glassy carbon electrode (GCE) and the GCE modified with $[Cu_2I_2(\mu\text{-pyrazine})]$. As illustrated in Fig. 5(a), the CV response of the unmodified GCE displays a weak redox peak, reflecting its inherently low electrocatalytic activity. In contrast, the $[Cu_2I_2(\mu\text{-pyrazine})]$-modified electrode exhibits a markedly enhanced redox current, indicating significantly improved electron transfer kinetics at the electrode–electrolyte interface. This enhancement can be attributed to the $[Cu_2I_2(\mu\text{-pyrazine})]$ complex, which facilitates greater conductivity and promotes efficient charge transport. As a result, the $[Cu_2I_2(\mu\text{-pyrazine})]$/GCE exhibits superior redox performance compared to the pristine electrode. Complementary EIS measurements were carried out over a frequency range of 0.05 Hz to 100 000 Hz with a 10 mV amplitude, providing deeper insights into the interfacial characteristics of the electrodes. At high frequencies, the impedance spectra reveal information related to the charge transfer resistance and double-layer capacitance, while the low-frequency region reflects ion diffusion processes. As depicted in Fig. 5(b), the Nyquist plot of the modified electrode shows a noticeably smaller semicircle diameter, indicating a substantial reduction in charge transfer resistance. This observation confirms that modification with $[Cu_2I_2(\mu\text{-pyrazine})]$ significantly accelerates the electron transfer rate, which contributes to a significant enhancement in the electrode's electrochemical performance.

The impact of scan speed on the electrochemical behavior of the $[Cu_2I_2(\mu\text{-pyrazine})]$-modified glassy carbon electrode ($[Cu_2I_2(\mu\text{-pyrazine})]$/GCE) was thoroughly examined using cyclic voltammetry (CV) in a 5 mM $[Fe(CN)_6]^{3-/4-}$ solution, as shown in Fig. 6(a). CV data were collected over a scan speed range of 20 to 180 mV s^{-1}. As the scan speed increased, both the positive and negative current peaks increased proportionally, indicating an accelerated diffusion of electroactive species toward the electrode surface. This behavior is consistent with a reversible electron transfer process, where the influence of kinetic limitations becomes more evident at higher scan speeds, ultimately enhancing the overall electrochemical performance of the electrode. As shown in Fig. 6(b), a linear correlation between the peak current and the square root of the scan rate ($\nu^{1/2}$) was observed, confirming that the electrochemical reaction at the $[Cu_2I_2(\mu\text{-pyrazine})]$/GCE surface is primarily governed by diffusion-controlled mass transport. These results, supported by both CV and EIS analyses, demonstrate that modification with $[Cu_2I_2(\mu\text{-pyrazine})]$ significantly enhances the electrode's electrochemical performance, underlining its promising potential for the development of efficient and sensitive electrochemical sensors. The effective electroactive surface areas of the unmodified glassy carbon electrode (GCE) and $[Cu_2I_2(\mu\text{-pyrazine})]$ functionalized GCE were determined through cyclic voltammetric analysis employing the Randles–Ševčík formalism (eqn (2)):[33]

$$I_p = (2.69 \times 10^5) \times n^{3/2} \times A \times D^{1/2} \times C \times \nu^{1/2} \quad (2)$$

Here, I_p represents the peak current (in amperes), n denotes the number of electrons involved in the redox process, A is the electroactive surface area (in cm^2), D refers to the diffusion coefficient of $[Fe(CN)_6]^{3-/4-}$ in 0.1 mol L^{-1} KCl (in cm^2 s^{-1}), ν is the scan rate (in V s^{-1}), and C corresponds to the analyte concentration in the bulk solution (in mol cm^{-3}).

The electrochemical behavior of 100 μM creatinine in 0.1 M phosphate-buffered saline (PBS, pH 7.4) was investigated using differential pulse voltammetry (DPV) with different electrode configurations. As illustrated in Fig. 7, the bare glassy carbon electrodes (GCEs) displayed weak and poorly defined oxidation peaks, indicating limited electrochemical activity toward

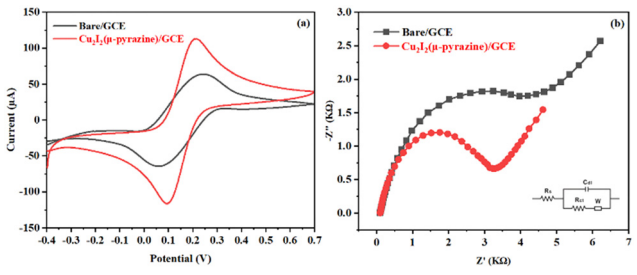

Fig. 5 (a) CV curves and (b) EIS spectra of bare/GCE and $[Cu_2I_2(\mu\text{-pyrazine})]$-modified GCE electrodes in a 5 mM $[Fe(CN)_6]^{3-/4-}$ solution containing 0.1 M KCl at a scan rate of 100 mV s^{-1}, conducted over a frequency range of 0.05 Hz to 100 000 Hz with a 10 mV amplitude.

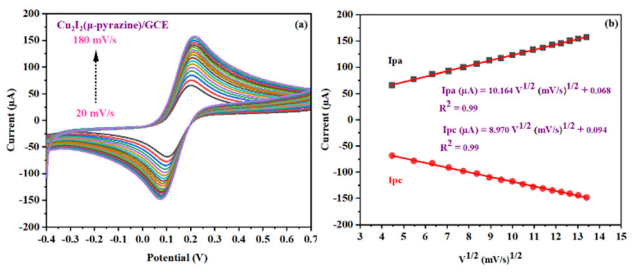

Fig. 6 (a) Cyclic voltammograms of the $[Cu_2I_2(\mu\text{-pyrazine})]$-modified electrode recorded in a 0.1 M KCl solution containing 5 mM $[Fe(CN)_6]^{3-/4-}$ at scan rates ranging from 20 to 180 mV s^{-1}. (b) Inset: Plot of redox peak current as a function of the square root of the scan rate.

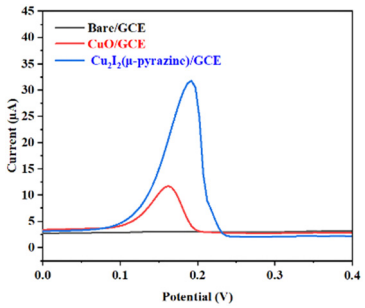

Fig. 7 Differential pulse voltammetry (DPV) of 100 μM creatinine at the bare GCE, CuO/GCE and [Cu_2I_2(μ-pyrazine)]/GCE in 0.1 M phosphate buffer solution PBS (pH = 7.4).

creatinine detection. Upon modification with CuO, a moderate increase in the oxidation current was observed, reflecting the intrinsic electrocatalytic activity of copper oxide. However, a much more pronounced enhancement was achieved with the [Cu_2I_2(μ-pyrazine)]-modified GCEs.

This significant improvement can be attributed to the increased electroactive surface area and the efficient electron transfer pathways offered by the [Cu_2I_2(μ-pyrazine)] complex. Its high electrical conductivity, favorable coordination environment, and excellent catalytic properties facilitate more effective interaction with creatinine molecules, resulting in amplified electrochemical responses. These results underscore the superior sensing performance of [Cu_2I_2(μ-pyrazine)] over CuO, highlighting its potential as a highly promising material for the sensitive and selective detection of creatinine in aqueous media.

The redox behavior of creatinine at the [Cu_2I_2(μ-pyrazine)]-modified electrode surface can be attributed to the electrocatalytic oxidation of the nitrogen-containing heterocycle within the creatinine structure. Differential pulse voltammetry (DPV) results (Fig. 7) reveal a distinct oxidation peak at approximately +0.85 V (*vs.* Ag/AgCl) for 100 μM creatinine in phosphate-buffered saline (pH 7.4), indicating a one-step irreversible oxidation process. The enhanced current response observed with [Cu_2I_2(μ-pyrazine)]/GCE compared to bare GCE and CuO/GCE confirms that the hybrid material promotes effective electron transfer and facilitates adsorption of creatinine through coordination with Cu(I) centers. Additionally, cyclic voltammetry (CV) measurements (Fig. 6) at varying scan rates show a linear relationship between the oxidation peak current and the square root of the scan rate, consistent with a diffusion-controlled mechanism. This suggests that the rate-limiting step involves the transport of creatinine to the electrode surface rather than charge transfer kinetics. The Cu–N coordination between creatinine and the hybrid complex likely lowers the activation energy required for oxidation, improving the electrocatalytic efficiency. These findings support a mechanism where creatinine is first adsorbed onto the electrode surface *via* interaction with Cu(I) sites, followed by electron loss from the guanidine moiety leading to oxidation and measurable current response.

The pH value of the metal ion solution significantly influences the voltammetric behavior of the sensor during the incubation process.[34] To evaluate this effect, the electrochemical performance of the sensor was examined across a pH range of 3–9 using differential pulse voltammetry (DPV). As shown in Fig. 5, the peak current exhibited a clear dependence on the electrolyte pH. Specifically, the influence of pH variations was assessed by studying the electrochemical behavior of the [Cu_2I_2(μ-pyrazine)] matrix during creatinine detection. On the other hand, the increased current observed at pH values above 7.4 is likely due to creatinine hydrolysis, which lowers the concentration of free creatinine, reducing their ability to interact with the sensor interface. Based on these observations, all subsequent electrochemical measurements were carried out in a 0.1 M phosphate buffer solution at pH 7.4 to ensure optimal sensitivity and reproducibility.

To investigate the influence of pH on the electrochemical behavior of the [Cu_2I_2(μ-pyrazine)]/GCE sensor, differential pulse voltammetry (DPV) measurements were carried out in phosphate buffer solutions with varying pH values. As illustrated in Fig. 8(c) (inset), the anodic peak potential (E_{pa}) exhibited a clear linear shift toward more positive values with increasing pH. This behavior indicates the direct involvement of protons in the redox reaction mechanism. A linear regression analysis yielded the equation: E_{pa} (V) = 0.0207 + 0.003pH, suggesting a redox process that involves an equal number of electrons and protons. This pH dependence highlights the proton-coupled electron transfer (PCET) nature of the redox system, providing further insight into the electrochemical mechanism of the sensor.

DPV-based analysis of creatinine

This observation highlights the effectiveness of [Cu_2I_2(μ-pyrazine)] as a highly sensitive material for the electrochemical detection of creatinine. As shown in Fig. 9(a), the DPV curve recorded for creatinine at the [Cu_2I_2(μ-pyrazine)]-modified glassy carbon electrode (GCE) demonstrates a direct proportional relationship between the oxidation peak current

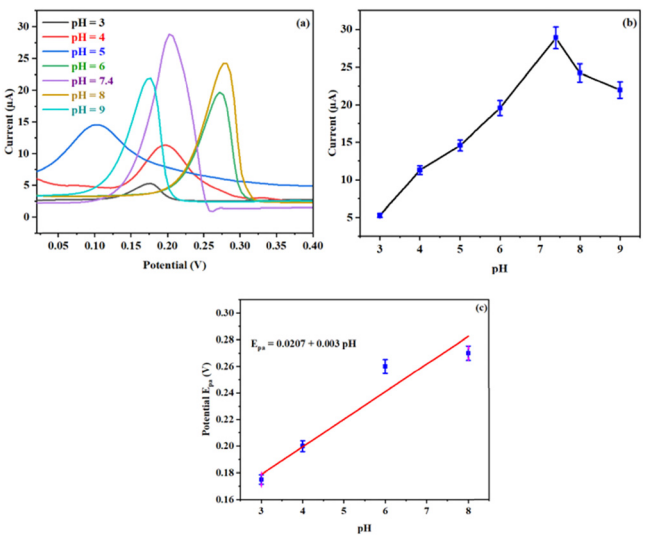

Fig. 8 (a) and (b) Effect of solution pH on the current response of creatinine at the [Cu_2I_2(μ-pyrazine)]/GCE electrode in 0.1 M phosphate buffer solution containing 100 μM creatinine. (c) Inset: Linear plot of E_{pa} *versus* pH.

and creatinine concentration, further illustrated by the calibration plot in Fig. 9(b). This relationship follows the linear regression equation I_{pa} (μA) = 17.643 log[creatinine] (μM) + 0.626, indicating excellent linearity. The sensor achieves an impressive detection limit of 1×10^{-8} M, confirming its outstanding sensitivity. Furthermore, Fig. 9(a) presents the DPV responses of the [Cu_2I_2(μ-pyrazine)]/GCE system across various creatinine concentrations, demonstrating the stability and reliability of the electrode modification over a wide dynamic range. Table 1 provides a comparison between the [Cu_2I_2(μ-pyrazine)]/GCE sensor and other electrochemical sensors previously reported for creatinine determination using differential pulse voltammetry (DPV). The comparison emphasizes key performance parameters, including linear detection range, detection limit, and electrode modification materials. The results demonstrate that the proposed sensor exhibits a competitive detection limit and a broad linear response range, outperforming many existing sensors. This enhanced performance is primarily attributed to the strong binding affinity of the [Cu_2I_2(μ-pyrazine)] complex toward creatinine and its excellent electron transfer capabilities. These findings confirm the sensor's high sensitivity, selectivity, and reliability positioning it as a promising platform for biological diagnostic applications.

Recent advances in electrochemical sensing have demonstrated the effectiveness of various copper-based materials such as metallic Cu, CuO, and CuO_2, as well as nanocomposites incorporating carbon-based frameworks like graphene, metal–organic frameworks (MOFs, and covalent organic frameworks) (COFs). For instance, CuO nanoparticles have been used for creatinine detection due to their redox activity, but they often suffer from poor selectivity in the presence of interfering species in biological matrices. Cu–graphene composites have shown improved electron transfer kinetics and higher surface areas, though their synthesis can be complex and often requires functionalization to enhance specificity. MOF- and COF-based sensors offer high porosity and tunable chemical functionality, but their limited electrical conductivity can necessitate the integration of conductive additives or polymer matrices. Compared to these materials, the [Cu_2I_2(μ-pyrazine)]/GCE sensor exhibits comparable or superior sensitivity, good recovery in real sample matrices, and ease of fabrication. Its structure offers favorable electronic properties while maintaining selectivity toward creatinine, making it a promising alternative for practical biosensing applications.

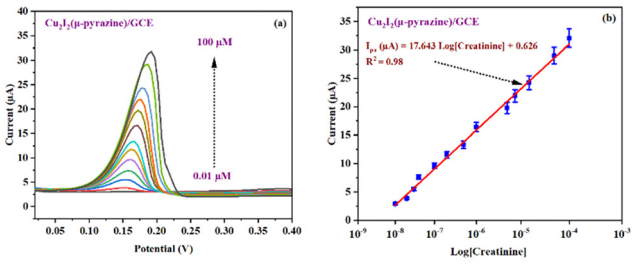

Fig. 9 (a) Differential pulse voltammetry (DPV) response of creatinine on various modified electrodes: [Cu_2I_2(μ-pyrazine)]/GCE, (b) corresponding calibration curves for creatinine using [Cu_2I_2(μ-pyrazine)]/GCE in 0.1 M phosphate buffer solution PBS pH = 7.4.

Interference study

To further evaluate the selectivity of the [Cu_2I_2(μ-pyrazine)]/GCE sensor, differential pulse voltammetry (DPV) responses were recorded both in the absence and presence of common interfering species, including uric acid (UA), ascorbic acid (AA), dopamine (DA), cysteine (Cys), and glucose, each at 100 μM. As illustrated in Fig. 10(a), the DPV response of 100 μM creatinine alone displays a well-defined oxidation peak at approximately +0.85 V. Upon addition of interfering species, the oxidation peak current of creatinine remained largely unchanged, with only minor fluctuations in current intensity (Fig. 10(b)). This comparison clearly demonstrates that the presence of these electroactive species does not significantly affect the signal for creatinine. The high selectivity of the sensor can be attributed to the specific coordination interaction between the nitrogen atoms of creatinine and the Cu(I) centers within the [Cu_2I_2(μ-pyrazine)] framework. This Cu–N interaction facilitates preferential adsorption and efficient electron transfer for creatinine compared to other interfering molecules, which either lack coordinating nitrogen atoms or do not form stable Cu–ligand complexes under the tested conditions. Additionally, the steric and electronic environment of the hybrid material likely favors the binding geometry and electrooxidation of creatinine, thereby enhancing both the sensor's sensitivity and selectivity.

Stability and reproducibility of the [Cu_2I_2(μ-pyrazine)]/GCE sensor

To evaluate the long-term operational stability of the [Cu_2I_2(μ-pyrazine)]-modified electrode, differential pulse voltammetry (DPV) measurements were performed over a period of 14 days under ambient storage conditions (room temperature, air exposure). The sensor was periodically tested in the presence of a fixed concentration of creatinine (100 μM) to monitor any changes in electrochemical response. As shown in Fig. 11(a) and (b), the sensor retained approximately 92.4% of its initial oxidation current after 7 days and 85.1% after 14 days. This gradual decline is likely attributed to partial oxidation or minor structural reorganization of the copper–iodide framework in an oxygen-rich environment. Nevertheless, the modified electrode maintained a robust and consistent response over the testing period, indicating good short-to-medium-term stability and supporting its practical applicability for routine creatinine monitoring. These findings underscore the importance of developing oxidation-resistant hybrid interfaces and motivate future studies involving longer-term assessments under different storage conditions.

The long-term performance and reproducibility of the [Cu_2I_2(μ-pyrazine)]/GCE sensor were evaluated by examining its electrochemical response toward a 100 μM creatinine solution. For repeatability assessment, a single [Cu_2I_2(μ-pyrazine)]-modified glassy carbon electrode (GCE) was used across multiple measurements,

Table 1 Analytical performance metrics of [Cu_2I_2(μ-pyrazine)]/GCE and other published platforms for creatinine detection

Modified electrode	Method	Linear range (μM)	LOD (μM)	Ref.
CuNPs/SPCE	CV	6–378	0.075	35
Iron(III) adsorbed within the paper	DPV	100–6500	43	36
MIP/Cu^{2+}	CV	10–100	0.06	37
Copper-oxide/ionic liquid/rGO	Amperometry	10–2000	0.22	38
GCE (based on Jaffe's reaction)	DPV	1–80	0.38	39
Screen printed carbon electrode (SPCE)	SWV	370–3600	8.6	40
CuO-IL/rGO/3DPE	Chronoamper-ometry	500–35 000	37.2	41
Pd/Cu_2O/PPy	DPV	0.1–150	0.05	42
[Cu_2I_2(μ-pyrazine)]/GCE	DPV	0.01–100	0.01	This work

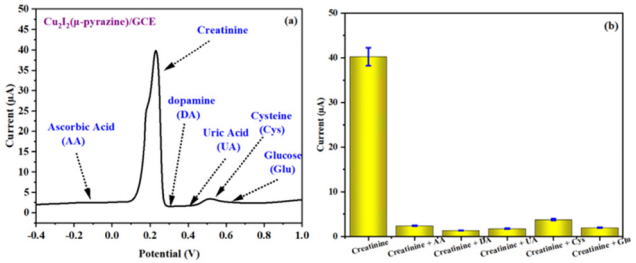

Fig. 10 DPV responses of the [Cu_2I_2(μ-pyrazine)]/GCE electrode toward 100 μM creatinine in 0.1 M phosphate buffer solution (PBS, pH 7.4), in the absence and presence of 100 μM common interfering species (AA, UA, Cys, DA, and glucose).

with consistent fabrication following a standardized modification protocol as shown in Fig. 11(c) and (d), only slight variations were observed in the oxidation peak current, with a relative standard deviation (RSD) of only 3.66%, demonstrating the excellent repeatability and reliability of the [Cu_2I_2(μ-pyrazine)]/GCE sensor. To evaluate reproducibility, four independently prepared [Cu_2I_2(μ-pyrazine)]/GCE electrodes, fabricated under identical conditions, were tested for their response to 100 μM creatinine in 0.1 M phosphate buffer solution (PBS) at pH 7.4 in Fig. 11(e) and (f). The results exhibited well-maintained oxidation peak currents, with a measured relative standard deviation (RSD) of 2.59%, confirming the high reproducibility of the [Cu_2I_2(μ-pyrazine)]/GCE sensor. The results confirmed both high repeatability and remarkable consistency of the sensor, demonstrating the reliability of the electrode fabrication process and the stability of the [Cu_2I_2(μ-pyrazine)] functional layer.

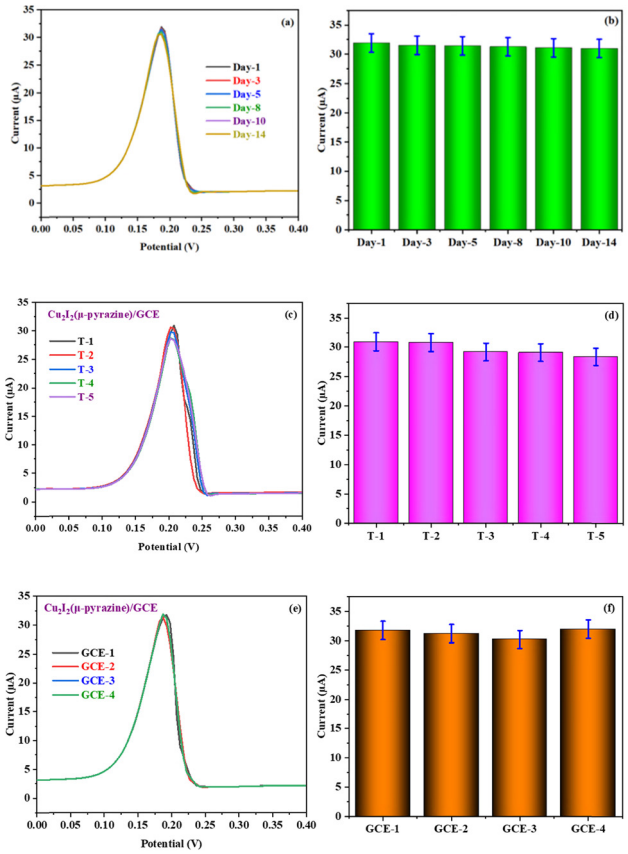

Fig. 11 Long-term stability of the [Cu_2I_2(μ-pyrazine)]/GCE sensor evaluated by DPV responses to 100 μM creatinine over a 14-day period (a) and (b). The repeatability and reproducibility of the sensor for detecting 100 μM creatinine were evaluated using [Cu_2I_2(μ-pyrazine)]/GCE-modified electrodes. For the repeatability test (c) and (d), measurements were performed using a single modified electrode, prepared through a consistent and uniform assembly protocol. To assess reproducibility (e) and (f), the sensor's response to 100 μM creatinine was recorded using four independently prepared [Cu_2I_2(μ-pyrazine)]/GCE electrodes in 0.1 M PBS at pH 7.4.

Practical application of the [Cu_2I_2(μ-pyrazine)]/GCE sensor

The practical applicability of the developed [Cu_2I_2(μ-pyrazine)]/GCE sensor was further evaluated through the analysis of real human serum samples. To minimize matrix effects and reduce the likelihood of electrode fouling, the serum was diluted 100-fold in 0.1 M phosphate-buffered saline (PBS, pH 7.4). Known concentrations of creatinine were then spiked into the diluted samples to generate test solutions within the linear range of the calibration curve. Differential pulse voltammetry (DPV) measurements were carried out on the diluted human serum samples both before and after spiking with known creatinine concentrations. As shown in Fig. S3, the DPV signal increased markedly upon spiking, whereas the unspiked sample exhibited only a weak baseline current. These observations not only confirm the presence of endogenous creatinine in the serum but also demonstrate the sensor's strong selectivity and minimal susceptibility to interference from other serum constituents. The concentrations determined at room temperature (RT)

Table 2 Determination of creatinine in real samples and its spiked recovery

Sample	Added (μM)	Found (μM)	Recovery (%)
Serum 1	1	0.95	95.0
	5	4.85	97.0
	10	9.03	90.3
	100	100.02	100.02
Serum 2	1	0.97	97.0
	5	5.1	102.0
	10	9.96	99.6
	100	103.9	103.9

are summarized in Table 2. As shown, the recovery rates ranged from 90.3% to 103.9%, underscoring the excellent accuracy and reproducibility of the method for creatinine detection in complex biological media. These results confirm that the proposed sensor is highly effective and suitable for practical real-sample applications, even under diluted serum conditions.

Conclusion

This study reports the synthesis, as well as the structural and optical characterization of a novel organic–inorganic hybrid material, [Cu_2I_2(μ-pyrazine)], prepared *via* a hydrothermal method. Optical measurements revealed a direct bandgap of 0.95 eV, indicating semiconducting behavior suitable for optoelectronic and sensing applications. To evaluate its biomedical potential, a [Cu_2I_2(μ-pyrazine)]-modified glassy carbon electrode (GCE) was fabricated as an electrochemical biosensor for the sensitive detection of creatinine, a critical biomarker for renal function monitoring. Electrochemical analyses, including cyclic voltammetry (CV) and impedance spectroscopy (EIS) confirmed enhanced redox kinetics and reduced charge transfer resistance, suggesting improved electron transfer efficiency and an increased electroactive surface area. The sensor displayed diffusion-controlled behavior and performed optimally at the physiological pH of 7.4. Differential pulse voltammetry (DPV) demonstrated a wide linear detection range (0.01–100 μM) with a low detection limit of 10 nM. The biosensor exhibited high selectivity toward creatinine in the presence of common interferents including uric acid (UA), ascorbic acid (AA), dopamine (DA), glucose, and cysteine. It also showed excellent repeatability and reproducibility (relative standard deviation $<4\%$). Real-sample analysis using human serum demonstrated high recovery rates (90.3–103.9%), confirming the sensor's accuracy, stability, and practical applicability in complex biological matrices. These findings highlight the potential of [Cu_2I_2(μ-pyrazine)] as a multifunctional material for the development of next-generation electrochemical biosensors, particularly in point-of-care diagnostics, clinical biochemistry, and health monitoring platforms.

Author contributions

Wissem Hallab: formal analysis, writing – original draft; Ahlem Guesmi: writing, investigation; Raja Jlassi: review & editing, visualization; Jassem Wannasi: formal analysis, writing; Noureddine Mhadhbi: software, data curation; Abdellah Tahiri: software, validation; Wesam Abd El-Fattah: formal analysis, validation; Naoufel Ben Hamadi: methodology, conceptualization; Houcine Barhoumi: supervision, Validation Houcine Naïli: project administration, validation, supervision.

Conflicts of interest

The authors declare that they have no known competing financial interests or personal relationships that could have appeared to influence the work reported in this paper.

Data availability

The data supporting this article have been included as part of the SI. See DOI: **https://doi.org/10.1039/d5tb01035g**.

CCDC 2422371 for [Cu_2I_2(μ-pyrazine)] contains the supplementary crystallographic data for this paper.[43]

Acknowledgements

This work was supported and funded by the Deanship of Scientific Research at Imam Mohammad Ibn Saud Islamic University (IMSIU) (grant number IMSIU-DDRSP2503).

Notes and references

1 V. V. Kovalev, Y. E. Gorbunova and Y. V. Kokunov, *Russ. J. Inorg. Chem.*, 2015, **60**, 886–888.
2 S. Xu, J. Wang, F. Zhao, H. Xia and Y. Wang, *J. Mol. Model.*, 2015, **21**, 1–10.
3 R. P. Houser, Z. Wang, D. R. Powell and T. J. Hubin, *J. Coord. Chem.*, 2013, **66**, 4080–4092.
4 G. H. Eom, H. M. Park, M. Y. Hyun, S. P. Jang, C. Kim, J. H. Lee, S. J. Lee, S. J. Kim and Y. Kim, *Polyhedron*, 2011, **30**, 1555–1564.
5 Y. K. S. J. Hong, J. Y. Ryu, J. Y. Lee, C. Kim and S. J. Kim, *Dalton Trans.*, 2004, 2697–2701.
6 M. A. S. Goher and F. A. Mautner, *Polyhedron*, 2000, **19**, 601–606.
7 A. J. Blake, N. R. Brooks, N. R. Champness, P. A. Cooke, M. Crew, A. M. Deveson, L. R. Hanton, P. Hubberstey, D. Fenske and M. Schröder, *Cryst. Eng.*, 1999, **2**, 181–195.
8 W. A. Lucas and F. Hou, *Cryst. Growth Des.*, 2022, **22**, 3128–3137.
9 J. Pospisil, I. Jess, C. Näther, M. Necas and P. Taborsky, *New J. Chem.*, 2011, **35**, 861–864.
10 N. M. Khatri, M. H. Pablico-Lansigan, W. L. Boncher, J. E. Mertzman, A. C. Labatete, L. M. Grande, D. Wunder, M. J. Prushan, W. Zhang, P. S. Halasyamani, J. H. S. K. Monteiro, A. De Bettencourt-Dias and S. L. Stoll, *Inorg. Chem.*, 2016, **55**, 11408–11417.
11 R. J. I. Shaik, A. Vohra and R. Devkar, *Eur. J. Chem.*, 2019, **10**, 131–138.

12 A. Das, I. Todorov, S. K. Dey and S. Mitra, *Inorg. Chim. Acta*, 2006, **359**, 2041–2046.
13 M. D. Allendorf and V. Stavila, *CrystEngComm*, 2015, **17**, 229–246.
14 Y. B. Dong, M. D. Smith, R. C. Layland and H. C. Zur Loye, *Chem. Mater.*, 2000, **12**, 1156–1161.
15 C. Jia, S. X. Liu, A. Neels, G. Labat and S. Decurtins, *Polyhedron*, 2005, **24**, 3032–3037.
16 B. F. Hoskins and R. Robson, *J. Am. Chem. Soc.*, 1990, 1546–1554.
17 M. A. Petrukhina, *Coord. Chem. Rev.*, 2007, **251**, 1690–1698.
18 P. Amo-Ochoa, O. Castillo and F. Zamora, *Dalton Trans.*, 2013, **42**, 13453–13460.
19 K. Sanderson, *Nature*, 2011, **469**, 18–20.
20 D. Rosiak, A. Okuniewski and J. Chojnacki, *Acta Crystallogr., Sect. C: Struct, Chem.*, 2018, **74**, 1650–1655.
21 J. S. Haynes, S. J. Rettig, J. R. Sams, J. Trotter and R. C. Thompson, *Inorg. Chem.*, 1988, **27**, 1237–1241.
22 N. S. Persky, J. M. Chow, K. A. Poschmann, N. N. Lacuesta, S. L. Stoll, S. G. Bott and S. Obrey, *Inorg. Chem.*, 2001, **40**, 29–35.
23 J. Wannassi, N. Missaoui, C. Mabrouk, H. Barhoumi, R. Crapnell, N. Jaffrezic-Renault and C. Banks, *J. Electrochem. Soc.*, 2023, **170**, 117504.
24 J. Wannassi, N. Missaoui, C. Tachouaft, C. Mabrouk, C. Autret-lambert, S. Bellali, F. Echouchene and H. Barhoumi, *J. Electrochem. Soc.*, 2024, **171**, 097511.
25 H. Khlifi, H. Wahbi, N. Mhadhbi, F. Saadi, E. Čižmár, A. Sánchez-Coronilla, F. Aouaini, B. Basha, N. Ben Hamadi, J. Wannassi, H. Barhoumi and H. Naïli, *J. Mol. Struct.*, 2025, **1333**, 141777.
26 J. Wannassi and F. Echouchene, *IEEE Int. Conf. Artif. Intell. Green Energy*, 2024, 1–4.
27 J. Wannassi, N. Missaoui, C. Mabrouk, C. A. Castilla-Martinez, Y. Moumen, F. Echouchene, H. Barhoumi, U. B. Demirci and H. Kahri, *ChemPlusChem*, 2025, **202**, 400734.
28 L. Yang, D. R. Powell and R. P. Houser, *J. Chem. Soc., Dalton Trans.*, 2007, 955–964.
29 J. T. Maeyer, T. J. Johnson, A. K. Smith, B. D. Borne, R. D. Pike, W. T. Pennington, M. Krawiec and A. L. Rheingold, *Inorg. Chem.*, 2003, **22**, 5121–5132.
30 M. Bazargan, M. Mirzaei and M. Akbari, *J. Mol. Struct.*, 2019, **1188**, 129–141.
31 C. Cappuccino, F. Farinella, D. Braga and L. Maini, *Cryst. Growth Des.*, 2019, **19**, 4395–4403.
32 S. Kawata, S. Kitagawa, H. Kumagai, S. Iwabuchi and M. Katada, *Inorg. Chim. Acta*, 1998, **267**, 143–145.
33 S. Carinelli, M. Luis-Sunga, J. L. González-Mora and P. A. Salazar-Carballo, *Chemosensors*, 2023, **11**, 533.
34 Y. Moumen, J. Wannassi, S. Bourigua, C. A. Castilla-Martinez and H. Barhoumi, *J. Electrochem. Soc.*, 2025, **172**, 027511.
35 J. Raveendran, P. E. Resmi, T. Ramachandran, B. G. Nair and T. G. Satheesh Babu, *Sens. Actuators, B*, 2017, **243**, 589–595.
36 E. L. Fava, T. M. do Prado, A. Garcia-Filho, T. A. Silva, F. H. Cincotto, F. Cruz de Moraes, R. C. Faria and O. Fatibello-Filho, *Talanta*, 2020, **207**, 120277.
37 T. Alizadeh and Z. Mousavi, *Microchim. Acta*, 2022, **189**, 1–11.
38 S. Boobphahom, N. Ruecha, N. Rodthongkum, O. Chailapakul and V. T. Remcho, *Anal. Chim. Acta*, 2019, **1083**, 110–118.
39 W. R. De Araújo, M. O. Salles and T. R. L. C. Paixão, *Sens. Actuators, B*, 2012, **173**, 847–851.
40 J. C. Chen, A. S. Kumar, H. H. Chung, S. H. Chien, M. C. Kuo and J. M. Zen, *Sens. Actuators, B*, 2006, **115**, 473–480.
41 K. Teekayupak, C. Aumnate, A. Lomae, P. Preechakasedkit, C. S. Henry, O. Chailapakul and N. Ruecha, *Talanta*, 2023, **254**, 124131.
42 R. S. A. Nagarajan and V. Sethuraman, *Anal. Methods*, 2023, **15**, 1410–1421.
43 W. Hallab, A. Guesmi, R. Jlassi, J. Wannassi, N. Mhadhbi, A. Tahiri, W. Abd El-Fattah, N. Ben Hamadi, H. Barhoumi and H. Naïli, CCDC 2422371: Experimental Crystal Structure Determination, 2025, DOI: **10.5517/ccdc.csd.cc2m9p0n**.